

# Abrupt Negative Thermal Expansion and Magnetic Structure of $V_3O_5$

Cintli Aguilar-Maldonado, Elena Solana-Madruga, Clemens Ritter, Olivier Mentré, and Ángel M. Arévalo-López\*



Cite This: *Chem. Mater.* 2022, 34, 5294–5300



Read Online

ACCESS |



Metrics & More

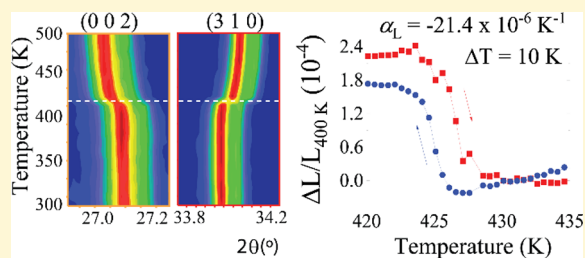


Article Recommendations



Supporting Information

**ABSTRACT:** We report bulk dilatometry and diffraction data through the  $T_{MIT} = 427$  K metal–insulator transition of the  $n = 3$  member of the  $V_nO_{2n-1}$  Magnéli series. Besides  $VO_2$ ,  $V_3O_5$  is the only other vanadium oxide with a potentially useful MIT transition above room temperature. A narrow ( $\Delta T = 10$  K) abrupt negative thermal expansion of  $\alpha_L = -21.4 \times 10^{-6}$  (dilatometric) and  $\alpha_V = -213 \times 10^{-6} K^{-1}$  (crystallographic) is observed. We argue that the combination of the MIT along with the simultaneous vanadium charge ordering is responsible for such large values. The low temperature magnetic properties are also clarified, and neutron diffraction measurements show a  $k = [1/2 \ 1/2 \ 0]$  magnetic structure at 1.5 K. DFT calculations of the exchange interactions support the low dimensionality and allow the modeling of the magnetic susceptibility.



The origin of the metal–insulator transition (MIT) in strongly correlated materials is a longstanding problem as the different possible causes often occur simultaneously. For instance, the archetypal  $VO_2$ ,<sup>1</sup> where electronic (Mott) and structural (Peierls) transitions occur at 340 K, or  $V_2O_3$ , with electronic, structural, and magnetic (Slater) transitions at 160 K,<sup>2</sup> are textbook examples. In addition, the transition of  $VO_2$  being above room temperature opens potential applications such as thermochromic windows, memory devices or optical switches.<sup>3–7</sup>

The only other, somehow underestimated, vanadium oxide that shows MIT above room temperature is  $V_3O_5$ . It belongs to the Magnéli series of oxides  $V_nO_{2n-1}$  ( $3 \leq n \leq 9$ ), which can be derived by ordered omission of chains of oxygen atoms and crystal shear planes along the  $[1-21]$  direction in the respective rutile end member  $VO_2$ .<sup>8,9</sup> The structures may also be viewed as slabs of  $n$ -octahedra long rutile-like units interconnected by  $V_2O_3$  sections as shown in Figure 1.<sup>10</sup> Most of these phases show an MIT along with a Peierls-like V–V dimerization inside the rutile-like edge sharing units, similar to  $VO_2$ . Their MITs are strongly influenced by the local metal–metal coordination, and the phase transitions arise as results of both electron lattice interactions within the  $VO_2$ -like and electronic correlations within the  $V_2O_3$ -like regions of the crystal.<sup>11</sup> However,  $V_3O_5$  ( $n = 3$ ), being a 1:1 mixture between  $VO_2$  and  $V_2O_3$  and with no clear dimerization at the MIT transition, deserves special attention.<sup>12,13</sup> The MIT of  $V_3O_5$  occurs at 427 K,<sup>14,15</sup> and it is accompanied by a structural transition from  $I$ -centered to primitive monoclinic symmetry ( $I2/c$  to  $P2/c$ ) and a charge ordering between  $V^{3+}$  and  $V^{4+}$  (see Figure 1b). The magnetism of  $V_3O_5$  is controversial, with a reported broad maximum in the susceptibility and a reduced

magnetic heat capacity (1.3% of the configurational spin entropy). It has been interpreted as one-dimensional (1D) correlations occurring at 76 K.<sup>16</sup>

In this paper, we revisit  $V_3O_5$  at both structural (high temperature) and magnetic (low temperature) transitions. We observe an overlooked and potentially useful abrupt negative thermal expansion occurring at the MIT via diffraction and dilatometric measurements. We unveil the spin structure with neutron diffraction at 1.5 K and clarify the dimensionality of the magnetic topology via DFT calculations obtaining the exchange interactions and modeling the magnetic susceptibility data.

## EXPERIMENTAL SECTION

Polycrystalline  $V_3O_5$  was synthesized from a stoichiometric mixture of  $VO_2$  and  $V_2O_3$  in a vacuum-sealed quartz ampule heated at 1150 °C for 24 h.  $V_2O_3$  was prepared from reduction of  $V_2O_5$  under hydrogen at 700 °C and  $VO_2$  from a 1:1  $V_2O_3$ : $V_2O_5$  mixture at 700 °C. X-ray diffraction (XRD) was performed on a Cu  $K_{\alpha 1}$  Bruker D8 Advance diffractometer on a Bragg–Brentano geometry in the  $5^\circ < 2\theta < 90^\circ$  range. Synchrotron XRD (SXR) was measured on cooling from 100 down to 10 K using the BL04 beamline at ALBA, Barcelona ( $\lambda = 0.413336$  Å). Neutron powder diffraction (NPD) data were collected at 1.5 and 80 K for 10 h at each temperature on a half gram pure sample using the D20 beamline at the ILL, Grenoble ( $\lambda = 2.41$  Å).

Received: April 5, 2022

Revised: May 9, 2022

Published: May 25, 2022



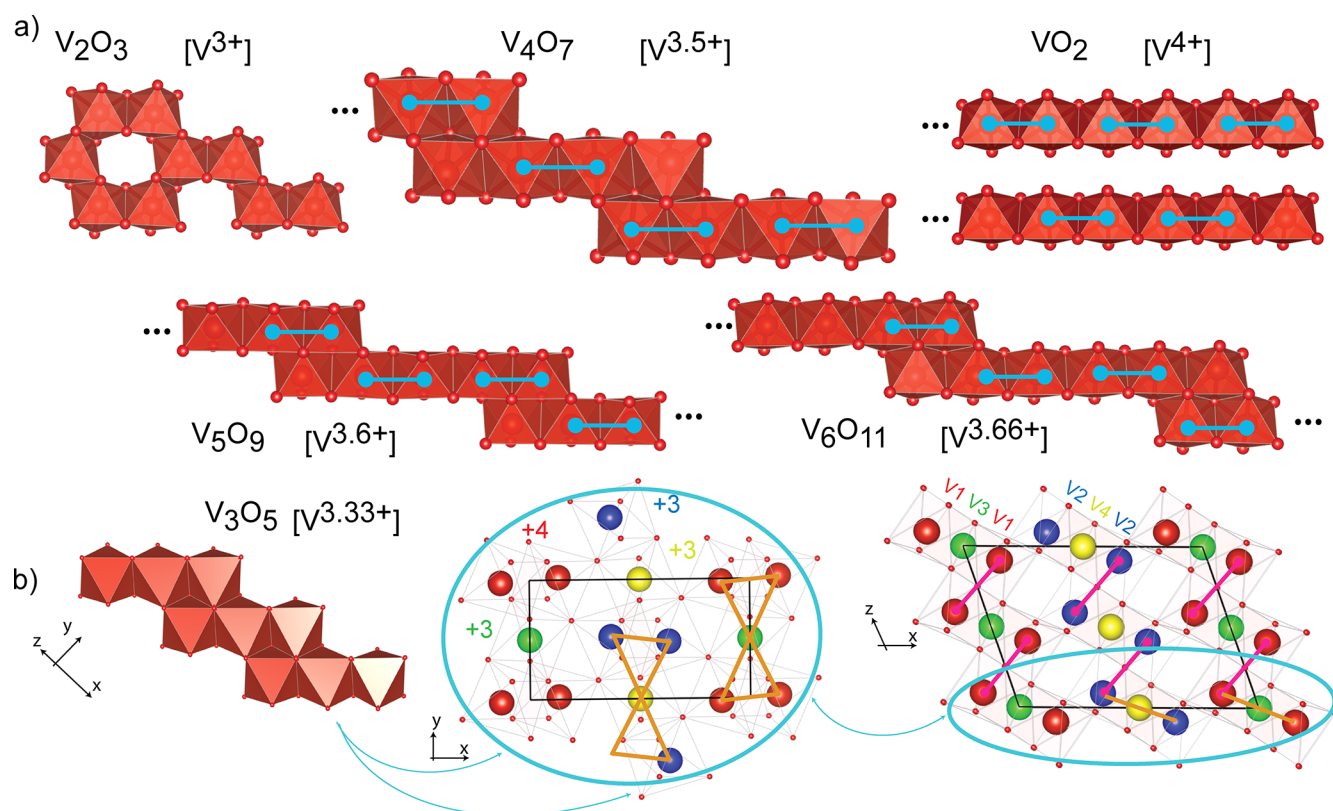


**Figure 1.** (a) Sections of the structures of  $VO_2$ ,  $V_2O_3$  and vanadium Magneli phases for  $n = 4, 5$ , and  $6$  along with their average oxidation state. The blue bonds represent the dimerization Peierls-like transition that the structures suffer at low temperatures along the rutile-like section. (b)  $[101]$ ,  $[001]$ , and  $[010]$  projections of the low temperature structure of  $V_3O_5$  where the  $n = 3$  rutile-like sections and the connections between them are highlighted as orange "bow-tie" chains. The pink bonds represent the linking between the different  $ab$  layers through face-shared octahedra stacking along  $c$ .

Rietveld refinement was done with FullProf Suite.<sup>17</sup> Mode analysis was made with the ISODISTORT internet-based tool.<sup>18,19</sup>

Magnetic measurements were performed on a Dynacool (9T) physical properties measurement system (PPMS) from Quantum Design. Zero field cooling (ZFC) and field cooling (FC) procedures between  $2 < T < 300$  K under a 0.1 T magnetic field were measured. Heat capacity was collected on the same system following a relaxation method. Resistivity measurements were collected on warming on a dense pellet using a Linkam chamber with the van der Paw method. Thermal expansion coefficient was measured using a Netzsch 402 C dilatometer.

DFT calculations were performed applying the local density approximation (LDA + U,  $U = 5$  eV) with the Perdew–Burke–Ernzerhof exchange–correlation potential using the Vienna ab initio simulation package (VASP) with the basis set of projected augmented waves on a  $3 \times 5 \times 4$   $k$ -mesh.<sup>20–22</sup> For the calculations of the magnetic exchanges identified in the text, we mapped the total energies for a number of collinear spin configurations onto a classical Heisenberg model to obtain individual exchange couplings and the effective on-site exchange interaction  $J_{eff} = 5$  eV in a  $5 \times 4 \times 3$  Monkhorst–Pack (MP) grid.

## RESULTS AND DISCUSSION

**Review of  $V_3O_5$ .** The structure of  $V_3O_5$  has been previously reported from single crystal diffraction data below (300 K, LT) and above (458 K, HT) its metal–insulator transition at  $T_{MIT} = 427$  K.<sup>12,13</sup> We report in Table 1 our Rietveld refinement in the LT phase from SXRD data collected at 10 K. The main difference between the LT ( $P2/c$  space group) and the HT ( $I2/c$  space group) modifications is the loss of the  $I$ -centering along with a charge ordering in one of

the two available positions at high temperature. Thus, the LT structure splits its mean  $V^{3.33+}$  valence from two into four independent vanadium sites with only one of them being in a 4+ oxidation state (V1 in Table 1). For the LT phase, Figure 1b shows the  $n = 3$  rutile-like edge-shared octahedra split in two different chains V1–V3–V1 and V2–V4–V2. These are inter-connected in the  $ab$  plane via corner sharing and intra-connected by edge sharing, defining a bow-tie in orange in Figure 1b. These  $ab$  double bow-tie planes are interconnected along  $c$  through V1–V1 (2.817(8) Å) and V2–V2 (2.763(8) Å) face-shared octahedra, see pink bonds in Figure 1b.

Figure 2a shows our Rietveld refinement of the room temperature XRD data of  $V_3O_5$ ; the presence of poorly crystallized  $VO_2$  secondary phase is marked with an asterisk. Figure 2b also shows the thermal evolution of the main diffraction maxima (002) and (310) through the transition at 427 K. The refined cell parameters (Figure 2c) show a clear anisotropic transition with  $a$  and  $b$  shrinking abruptly on warming while  $c$  and  $\beta$  expand.

The transition from the LT to the HT phase shows an abrupt discontinuity at  $T_{MIT}$  leading to a narrow overall negative thermal expansion (NTE) of the lattice volume as shown in Figure 3a. The expansion coefficient  $\alpha_V = \Delta V / (V\Delta T)$  reaches  $-213 \times 10^{-6} K^{-1}$  in a 10 K range, comparable to the colossal NTE value of  $-410 \times 10^{-6} K^{-1}$  in a 70 K range observed in  $Bi_{0.95}La_{0.05}NiO_3$ .<sup>23</sup> In the later compound, these large values result from the volume collapse at the metal–insulator along with charge-transfer transitions. However, the origin of such NTE values in  $V_3O_5$  arises from the MIT and

**Table 1. Structural Parameters and Bond Valence Sums (BVS) of  $V_3O_5$  from Data Collected at 10 K from SXRD ( $R_{\text{Bragg}} = 4.74\%$ )<sup>a</sup>**

atom	site	x	y	z	BVS
V1	4g	0.1314(3)	0.0074(6)	0.4109(6)	+3.9(1)
V2	4g	0.3709(3)	0.4971(6)	0.0910(6)	+2.9(1)
V3	2c	0	1/2	0	+3.0(1)
V4	2d	1/2	0	0	+3.0(1)
O1	4g	0.3007(9)	0.146(1)	0.462(1)	-2.2(1)
O2	4g	0.1856(9)	0.339(1)	0.026(1)	-2.0(1)
O3	4g	0.082(1)	0.151(1)	0.636(1)	-1.9(1)
O4	4g	0.420(1)	0.343(1)	0.862(1)	-1.9(1)
O5	2e	0	0.297(1)	1/4	-1.9(1)
O6	2f	1/2	0.185(1)	1/4	-1.9(1)

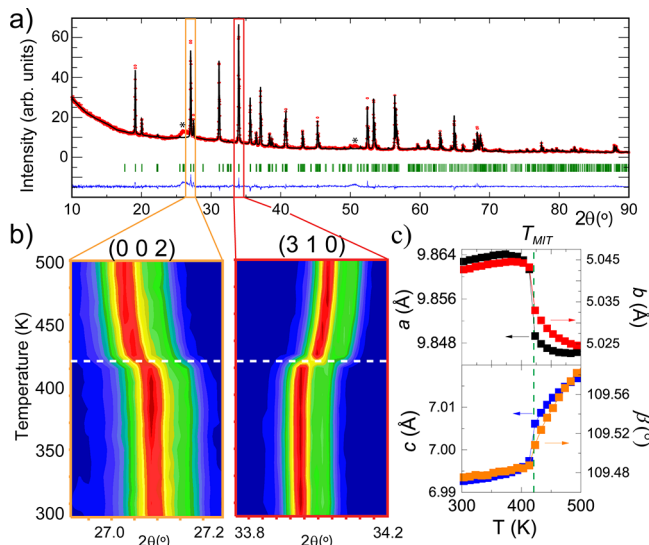
  

bond	Å	bond	Å	bond	Å
V1–O1	1.73(1)	V1–O3	1.94(1)	V1–O3	1.98(1)
V1–O2	1.92(1)	V1–O3	2.17(1)	V1–O5	2.02(3)
V2–O1	2.03(1)	V2–O4	1.98(1)	V2–O4	1.97(1)
V2–O2	1.90(1)	V2–O4	2.13(1)	V2–O6	2.09(1)
V3–O2 x2	1.95(1)	V3–O3 x2	2.03(1)	V3–O5 x2	2.02(1)
V4–O1 x2	2.03(1)	V4–O4 x2	2.01(1)	V4–O6 x2	1.98(1)

	$\mu_x$	$\mu_y$	$\mu_z$	total ( $\mu_B$ )
V1 (4+)	0	0.47(4)	0.47(4)	0.67(6)
V2 (3+)	0	-0.38(2)	0.98(1)	1.05(5)
V3 (3+)	0	-1.17(4)	0.53(1)	1.28(4)
V4 (3+)	0	1.17(4)	0.53(1)	1.28(4)

<sup>a</sup>The Bottom Part Shows the Magnetic Moments Obtained from NPD Data at 1.5 K ( $R_{\text{mag}} = 14.2\%$ ). Refined in  $P2_1/c$ ,  $a = 9.85884(3)$  Å,  $b = 5.03439(1)$  Å,  $c = 6.99456(2)$  Å,  $\beta = 109.4616(1)^\circ$ .



**Figure 2.** (a) Rietveld refinement for XRD of  $V_3O_5$ . Asterisks represent the main reflection of  $VO_2$ , presented as poorly crystallized secondary phase. (b) High-temperature XRD of (002) and (310) main reflections of  $V_3O_5$  with a clear transition at  $T_{MIT} = 427$  K. (c) Thermal evolution of the cell parameters that evidences the anisotropy of the transition.

vanadium charge-ordering transition. This is confirmed by the thermal variation of interpolated BVS in Figure 3a where a critical variation in charge states is seen from  $\sim 350$  K up to  $T_{MIT}$ . The main effect is the formation of the short vanadyl bond V1–O1 ( $\sim 1.7$  Å) along with the V–V distance change in the rutile–trimers (in the  $ab$  plane) from the equivalent

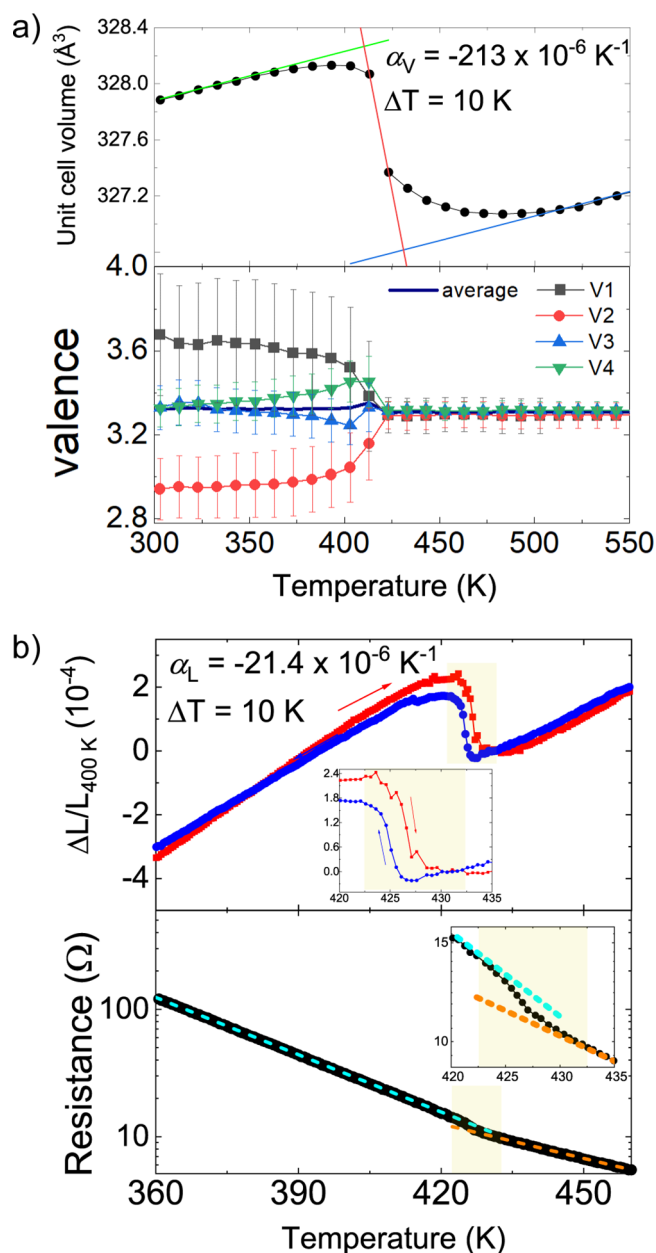


**Figure 3.** (a) Thermal evolution of the unit cell volume (top) and the BVS (bottom) for the vanadium atoms in  $V_3O_5$ . (b) Dilatometric linear thermal expansion of  $V_3O_5$  on heating and cooling (top) showing a 2 K hysteresis and temperature dependence of the electrical resistance (bottom) in a semi-log scale. Insets show the transition.

2.93(2) Å at 440 K to 2.83(2) and 3.05(2) Å at 400 K for V1–V3 and V2–V4, respectively. The evolution of the cell parameters and the volume in the LT phase in the 10–100 and 300–420 K temperature range is presented in the Supporting Information.

Dilatometric measurements on a polycrystalline pellet of  $V_3O_5$  were made under heating and cooling cycles as shown in Figure 3b. The strain  $\Delta L/L_0$  ( $L_0$  are the values at 400 K) increases with increasing temperature up to 420 K indicating the standard positive thermal expansion but decreases above 420 K. The average observed linear thermal expansion coefficient  $\alpha_L$  between 420 and 430 K is  $-21.4 \times 10^{-6} \text{ K}^{-1}$ . This value is close to the NTE (GNTE) of  $-25 \times 10^{-6} \text{ K}^{-1}$  observed also by dilatometry in the anti-perovskite manganese

nitride  $(\text{Mn}_{0.96}\text{Fe}_{0.04})_3(\text{Zn}_{0.5}\text{Ge}_{0.5})\text{N}$  ceramic over a 70 K temperature range.<sup>24</sup> The derived bulk thermal expansion is only about 30% of the crystallographic value ( $^{1/3}\alpha_V = 71 \times 10^{-6} \text{ K}^{-1}$ ), suggesting that  $\text{V}_3\text{O}_5$  ceramics showing GNTE should be accessible through further materials processing, such as reduction of the particle size, minimizing pore formation.<sup>25</sup> A hysteresis of 2 K is observed between warming and cooling cycles.

The MIT transition in  $\text{V}_3\text{O}_5$  has been previously established at 427 K through resistivity measurements in single crystals.<sup>14</sup> Our own measurements on a sintered pellet of  $\text{V}_3\text{O}_5$  are shown in Figure 3b. However, grain boundary resistances preclude a clear picture of the MIT transition and only a change in the slope at the correct temperature was observed.

The thermal dependence of the magnetic susceptibility is shown in Figure 4a. The Curie–Weiss fit was possible only above 275 K (see Supporting Information), resulting in a  $\mu_{\text{eff}} = 2.50(1) \mu_B$  per V. Although this value should be taken with caution, it agrees well with the expected value of  $\mu_{\text{theo}} = 2.51 \mu_B$

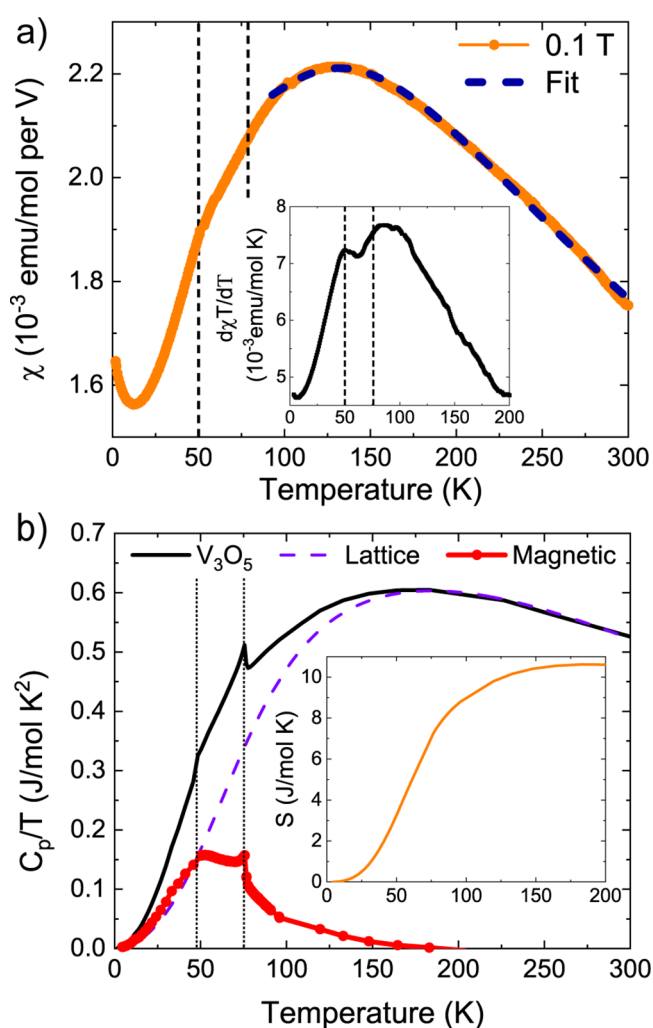


**Figure 4.** (a) Magnetic susceptibility of  $\text{V}_3\text{O}_5$ . The fit follows the equation described in the text. The inset shows the Fisher's heat capacity ( $d\chi T/dT$  vs  $T$ ) showing two transitions at 50 and 76 K. (b) Thermal evolution of the specific heat divided by temperature showing two clear magnetic transitions at 76 and 50 K after subtraction of the lattice contribution. The inset shows the calculated magnetic entropy reaching 44% of the ideal value for  $\text{V}_3\text{O}_5$ .

per  $\text{V}^{3.33+}$  for  $\text{V}_3\text{O}_5$ . It is also in accordance with the measurements performed on single crystals and their reported fit in the 290–700 K temperature range.<sup>14</sup> The low temperature region fit was only performed after knowledge of the magnetic structure, considering the interplay between magnetic exchanges deduced from DFT calculations as described later.

The inset of Figure 4a shows Fisher's heat capacity  $d(\chi T)/dT$  where two maxima at  $T_N = 76$  K and a previously unidentified transition at 50 K are observed. These two transitions are also observed in the magnetic contribution of the heat capacity as presented in Figure 4b. The recovered magnetic entropy reaches its saturation at 200 K ( $\sim 10$  J/mol K) but represents only about 44% of the expected configurational spin entropy  $\Delta S = R(2\ln 3 + \ln 2) = 24$  J/mol K for  $2 \times \text{V}^{3+}$  ( $S = 1$ ) and one  $\text{V}^{4+}$  ( $S = 1/2$ ). These results suggest the setting of significant low-dimensional spin correlations at high temperatures.

The magnetic structure of  $\text{V}_3\text{O}_5$  has been solved via neutron powder diffraction (NPD) using a difference pattern between 10 h long collections at 1.5 and 80 K as shown in Figure 5a. No attempt was made to obtain neutron diffraction in between the two magnetic transitions due to long collection times and small ordered moment at high temperatures. All the magnetic diffraction maxima at 1.5 K can be indexed with the  $k = [1/2, 1/2, 0]$  propagation vector. The best fit to the data was obtained with the mC2- irreducible representation in a  $\{(-2, 0, 0), (0, 2, 0), (0, 0, -1)\}$  supercell with the monoclinic  $C2/c$  magnetic space group (15.91,  $R_{\text{mag}} = 14.2\%$ ) using ISODISTORT and FullProf. The magnetic structure is non collinear and consists of four independent vanadium sites with the moments confined in the  $bc$  plane and refining to 0.67(6), 1.05(5), 1.28(4), and 1.28(4)  $\mu_B$  for V1, V2, V3, and V4 in Table 1, respectively (V3 and V4 reached equal values and therefore constrained for final refinements). These values agree with the charge ordering ( $T_{\text{MIT}} = 427$  K), showing the lowest moment for V1, the vanadium in a 4+ oxidation state, see Figure 5b.

The spin structure can be understood starting with the layers confined in the  $ab$  plane and the “bow-tie” chains described in the structural part, see Figure 1b. These “bow-tie” sublattices show intrinsically the same order with V1–V1 (V2–V2) being AFM coupled and the central linker V3 (V4) being frustrated. All together, they form V1–V1–V2–V2–V1–V1 antiferromagnetic chains with V3 and V4 as ferromagnetic linkers along  $a$  between them, see red (AFM) and blue (FM) thick bonds in Figure 5b. The coupling between these layers is through the face sharing octahedra, see Figure 1b.

In order to understand the magnetic structure of  $\text{V}_3\text{O}_5$ , the spin exchange interactions were examined via DFT + U calculations. To keep the number of interactions meaningful, an  $ab$  layered structure was finally considered with five different in-plane exchange interactions ( $J1$ – $J5$ ) and one interlayer coupling ( $J_{\text{inter}}$ ). Several magnetic configurations were calculated in a charge-ordered  $b$ -doubled unit cell, resulting in local magnetic moments in agreement with  $S = 1/2$  and  $S = 1$  for  $\text{V}^{4+}$  and  $\text{V}^{3+}$ , respectively (see Supporting Information). However, for the exchange couplings calculations, all magnetic sites have been assigned to an average  $n = 5/3$  electron filling in accordance to the  $\text{V}^{3.33+}$  mean valence. Thus, the vanadium charge-ordered state was not directly considered and the couplings considered as equal were V1–V1 ( $J3'$ ) = V2–V2 ( $J3''$ ), V1–V3 ( $J4'$ ) = V2–V4 ( $J4''$ ), V1–V4 ( $J2'$ ) = V2–V3 ( $J2''$ ), and V1–V1 ( $J_{\text{inter}}'$ ) = V2–V2 ( $J_{\text{inter}}''$ ), see Figure 5c,d.

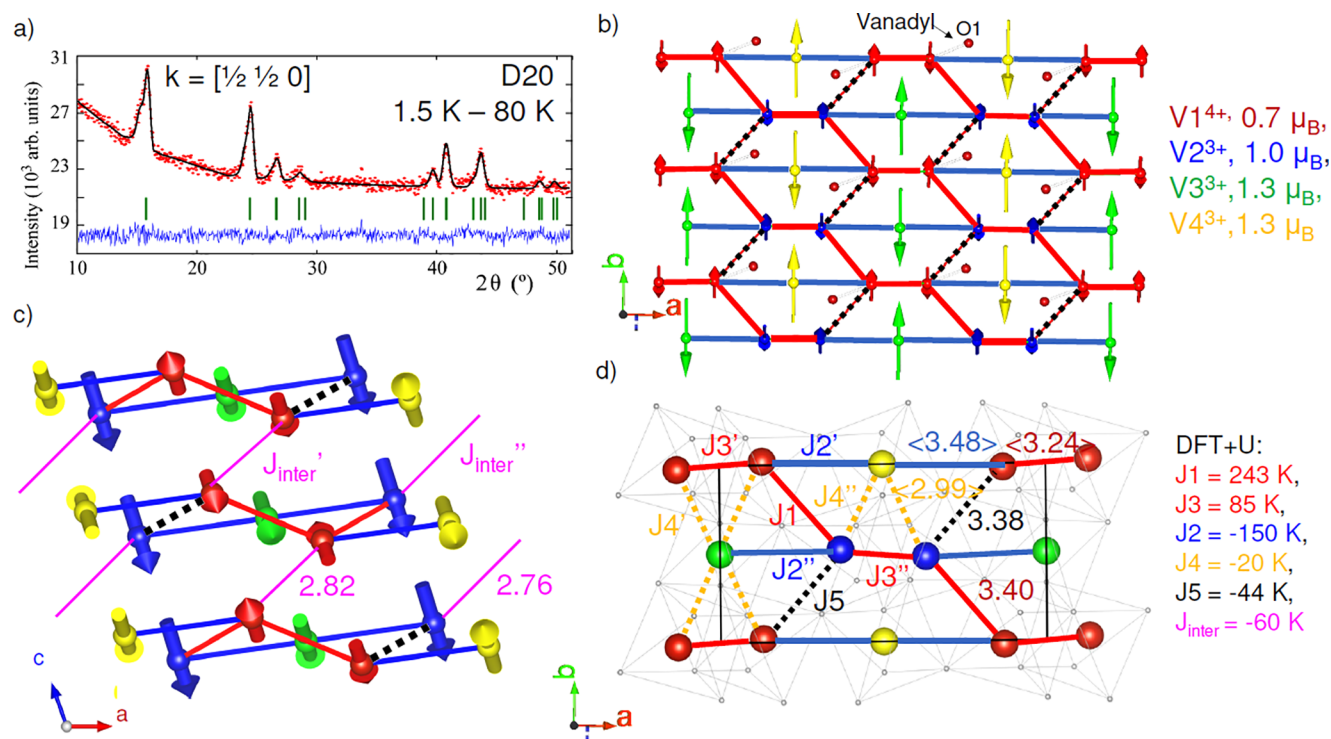


**Figure 5.** Magnetic structure of  $V_3O_5$ . (a) Rietveld fit to the NPD 1.5–80 K difference pattern. (b) [001] view of the refined magnetic structure of  $V_3O_5$  from (a) along with the magnetic moments for each vanadium. Small red spheres represent O1 and their vanadyl bond. Red/Blue thick bonds are the strongest AFM/FM interactions. Broken black bond represents the V–V bond involving the vanadyl short V1–O1 distance. (c) Magnetic structure along the [010] with the exchange interaction in between layers  $J_{inter}$ . (d) Average between primed and double-primed relevant V–V distances and  $J$  exchange interactions calculated from DFT in the low temperature structure of  $V_3O_5$ , see text for details. Red/blue/green/yellow spheres/spins are for V1/V2/V3/V4, respectively.

The relevant distances, the exchange interactions, and the magnetic structure are shown in Figure 5. The three main in-plane interactions ( $J_1 = 243$  K,  $J_2 = -150$  K, and  $J_3 = 85$  K) form a system of linear alternating antiferromagnetic chains ( $J_1$ – $J_3$ – $J_1$ ) coupled ferromagnetically ( $J_2$ ); these agree with the experimental magnetic structure described above. Although bond lengths between  $J_1$  and  $J_5$  are very similar (3.40 Å vs 3.38 Å), the exchange interactions are more than five times apart and of the opposite sign (243 K vs –44 K); such a difference is striking but explained by the short vanadyl bond present in the  $V^{4+}$  (V1–O1, 1.72 Å) as seen in Figure 5b. It has been previously established that the magnetic orbital of a  $V^{4+}$  in a solid with vanadyl bond is contained in the  $d_{xy}$  orbital, in the equatorial plane of the (1–4–1) vanadium octahedron, i.e., perpendicular to the short and the long bonds (1.72 and 2.17 Å).<sup>26</sup> Thus, the exchange path through the V1–O1 bond is mainly canceled, since the overlap with the apical oxygen  $p$ -orbital is almost zero. This bond appears at the MIT transition and along with the vanadium charge ordering; they are responsible for the negative thermal expansion.

Considering the two-dimensional magnetic structure obtained from NPD and confirmed by DFT, the low temperature magnetic susceptibility was modeled. In the low temperature region, a broad maximum is observed around  $\sim 125$  K and evidences the low dimensional behavior, previously interpreted as 1D spin correlations.<sup>16</sup> The magnetic susceptibility was thus fitted above the long range magnetic ordering in the  $100 \text{ K} < T < 300 \text{ K}$  temperature range with the analytical expression  $\chi_{chain}(T)$  for an alternating AFM chain  $J_1$ – $J_3$  with dominating dimers ( $0.35 J_1 \approx J_3$  from DFT values) as reported by Hatfield and Kahn.<sup>27,28</sup> The V3 and V4 spins

(i.e., 1/3rd of the total spin content) were considered as a paramagnetic independent contribution but interacting with the chains through a Curie–Weiss term called  $\theta_2$  below. The interchain spin-exchange interaction was allowed in the molecular field expansion with  $\theta_{inter} = (zS(S+1)/3)(J_{inter}/k_B)$ , with the number of surrounding chains  $z = 4$ : 2 in-plane, 2 apical. Thus, the observed susceptibility was modeled with the following expression for  $S = 1$  (see SI for full details):

$$\chi = \frac{2}{3} \left( \frac{\chi_{chain}(T)}{1 - \theta_{inter} \left[ \frac{\chi_{chain}(T)}{C} \right]} \right) + \frac{1}{3} \left( \frac{C_2}{T - \theta_2} \right) + \text{TIP} \quad (1)$$

The fit results in  $J_1 = 326(2)$  K and  $J_{inter} = -40(1)$  K, which are in good agreement with the DFT values and confirm the FM coupling between the chains.  $\theta_2 = -132(2)$  K implies a  $J_{\theta_2} \approx -50$  K (AFM), opposite to what is expected; however, this represents the average interaction in between the layers, which is still small compared with the considered in-plane interactions and outside the energy scale of the concerned low dimensional topology above the transition.

## CONCLUSIONS

Judging from the already gained experience in applications of  $VO_2$ ,  $V_3O_5$  is a potentially useful material at high temperatures, serving as an ideal playground for expanding uses already known. For instance, very recently,  $V_3O_5$  has been tested for volatile resistive switching and showed promising behavior for neuromorphic computing.<sup>29</sup> Moreover, the abrupt negative thermal expansion due to the  $ab$  plane revealed in here

enlarges the possibilities of  $V_3O_5$ . In contrast,  $VO_2$  does show some anisotropy in its structural behavior but with an overall positive thermal expansion through its MIT.<sup>30</sup> Although the NTE values reported for  $V_3O_5$  are for a narrow temperature range ( $\alpha_V = -213 \times 10^{-6} \text{ K}^{-1}$  and  $\alpha_L = -21.4 \times 10^{-6} \text{ K}^{-1}$  for a  $\Delta K = 10 \text{ K}$ ), known strategies may help to broaden the transition as observed in the Ge-doped anti-perovskite nitrides.<sup>21,31</sup> The mechanisms behind the NTE in  $V_3O_5$  are the MIT along with the charge-ordering of the vanadium atoms. The MIT is solely responsible of the NTE for instance in  $V_2O_3$ ,<sup>32</sup> and charge-ordering has only recently been identified as a key factor for the NTE of  $V_2OPO_4$ .<sup>33</sup> The mixing of both behaviors is probably responsible for the NTE values observed here.

At low temperatures,  $V_3O_5$  shows a broad maximum in the magnetic susceptibility, which is now identified as a 2D behavior. The exchange interactions obtained from DFT model correctly the susceptibility and are also in accordance with the magnetic structure from NPD collected at 1.5 K. This consists of *ab* planes formed by AFM chains coupled FM. The 2D correlations are likely to start below the  $T_{MIT}$  with the same *ab* plane being responsible of the NTE in  $V_3O_5$ .

## ■ ASSOCIATED CONTENT

### SI Supporting Information

The Supporting Information is available free of charge at <https://pubs.acs.org/doi/10.1021/acs.chemmater.2c01030>.

Additional crystallographic parameters, additional graphics, and details for the DFT magnetic configurations (PDF)

## ■ AUTHOR INFORMATION

### Corresponding Author

Ángel M. Arévalo-López – Univ. Lille, CNRS, Centrale Lille, Univ. Artois, UMR 8181 – UCCS – Unité de Catalyse et Chimie du Solide, F-59000 Lille, France; [orcid.org/0000-0002-8745-4990](https://orcid.org/0000-0002-8745-4990); Email: [angel.arevalo-lopez@univ-lille.fr](mailto:angel.arevalo-lopez@univ-lille.fr)

### Authors

Cintli Aguilar-Maldonado – Univ. Lille, CNRS, Centrale Lille, Univ. Artois, UMR 8181 – UCCS – Unité de Catalyse et Chimie du Solide, F-59000 Lille, France; CRISMAT, UMR CNRS 6508, ENSICAEN, Université de Caen Basse-Normandie, 14050 Caen, France; [orcid.org/0000-0001-7229-6216](https://orcid.org/0000-0001-7229-6216)

Elena Solana-Madruga – Univ. Lille, CNRS, Centrale Lille, Univ. Artois, UMR 8181 – UCCS – Unité de Catalyse et Chimie du Solide, F-59000 Lille, France; Departamento de Química Inorgánica, Facultad CC. Químicas, Universidad Complutense de Madrid, 28040 Madrid, Spain; [orcid.org/0000-0001-6175-6053](https://orcid.org/0000-0001-6175-6053)

Clemens Ritter – Institut Laue-Langevin, 38042 Grenoble Cedex, France

Olivier Mentré – Univ. Lille, CNRS, Centrale Lille, Univ. Artois, UMR 8181 – UCCS – Unité de Catalyse et Chimie du Solide, F-59000 Lille, France; [orcid.org/0000-0002-1822-6003](https://orcid.org/0000-0002-1822-6003)

Complete contact information is available at: <https://pubs.acs.org/doi/10.1021/acs.chemmater.2c01030>

## Author Contributions

The study was designed by A.M.A.L. Synthesis, measurements, and analysis were performed by C.A.M., E.S.M., and A.M.A.L. NPD was performed and analyzed by C.R. DFT was calculated by O.M. The manuscript was written by A.M.A.L. with contributions of all authors.

## Funding

We thank support from ANR AMANTS project (19-CE08-0002-01) and the ILL and ALBA for granting us with beamtime.

## Notes

The authors declare no competing financial interest.

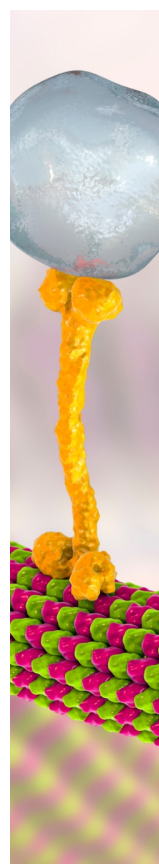
## ■ ACKNOWLEDGMENTS

The Chevreul Institute (FR 2638), Region Hauts-de-France, and FEDER are acknowledged for funding the X-ray diffractometers, the “LEGO” multianvil-press, and the PPMS magnetometer.

## ■ REFERENCES

- (1) Morin, F. J. Oxides Which Show a Metal-to-Insulator Transition at the Neel Temperature. *Phys. Rev. Lett.* **1959**, *3*, 34–36.
- (2) McWhan, D. B.; Menth, A.; Remeika, J. P.; Brinkman, W. F.; Rice, T. M. Metal-Insulator Transitions in Pure and Doped  $V_2O_3$ . *Phys. Rev. B* **1973**, *7*, 1920–1931.
- (3) Nakano, M.; Shibuya, K.; Okuyama, D.; Hatano, T.; Ono, S.; Kawasaki, M.; Iwasa, Y.; Tokura, Y. Collective Bulk Carrier Delocalization Driven by Electrostatic Surface Charge Accumulation. *Nature* **2012**, *487*, 459–462.
- (4) Driscoll, T.; Kim, H. T.; Chae, B. G.; Kim, B. J.; Lee, Y. W.; Jokerst, N. M.; Palit, S.; Smith, D. R.; Di Ventra, M.; Basov, D. N. Memory Metamaterials. *Science* **2009**, *325*, 1518–1521.
- (5) Zheludev, N. I.; Kivshar, Y. S. From Metamaterials to Metadevices. *Nat. Mater.* **2012**, *11*, 917–924.
- (6) Ke, Y.; Wang, S.; Liu, G.; Li, M.; White, T. J.; Long, Y. Vanadium Dioxide: The Multistimuli Responsive Material and Its Applications. *Small* **2018**, *14*, 1802025.
- (7) Brahlek, M.; Zhang, L.; Lapano, J.; Zhang, H. T.; Engel-Herbert, R.; Shukla, N.; Datta, S.; Paik, H.; Schlom, D. G. Opportunities in Vanadium-Based Strongly Correlated Electron Systems. *MRS Commun.* **2017**, *7*, 27–52.
- (8) Horiuchi, H.; Morimoto, N.; Tokonami, M. Crystal Structures of  $V_nO_{2n-1}$  ( $2 \leq n \leq 7$ ). *J. Solid State Chem.* **1976**, *17*, 407–424.
- (9) Kosuge, K. *Chemistry of Non-Stoichiometric Compounds*; Oxford University Press: 1994, DOI: [10.1093/oso/9780198555551.001.0001](https://doi.org/10.1093/oso/9780198555551.001.0001).
- (10) Bursill, L. A.; Hyde, B. G. Crystallographic Shear in the Higher Titanium Oxides: Structure, Texture, Mechanisms and Thermodynamics. *Prog. Solid State Chem.* **1972**, *7*, 177–253.
- (11) Schwingenschlögl, U.; Eyert, V. The Vanadium Magnéli Phases  $V_nO_{2n-1}$ . *Ann. Phys.* **2004**, *13*, 475–510.
- (12) Åsbrink, S. The Crystal Structure of and Valency Distribution in the Low-Temperature Modification of  $V_3O_5$ . The Decisive Importance of a Few Very Weak Reflexions in a Crystal-Structure Determination. *Acta Crystallogr., Sect. B: Struct. Crystallogr. Cryst. Chem.* **1980**, *36*, 1332–1339.
- (13) Hong, S. H.; Åsbrink, S. The Structure of the High-Temperature Modification of  $V_3O_5$  at 458 K. *Acta Crystallogr. Sect. B Struct. Crystallogr. Cryst. Chem.* **1982**, *38*, 713–719.
- (14) Jhans, H.; Honig, J. M. The Resistivity and Magnetic Susceptibility of  $V_3O_5$  Single Crystals. *J. Solid State Chem.* **1981**, *38*, 112–115.
- (15) Andreev, V. N.; Klimov, V. A. Specific Features of Electrical Conductivity of  $V_3O_5$  Single Crystals. *Phys. Solid State* **2011**, *53*, 2424–2430.

- (16) Griffing, B. F.; Faile, S. P.; Honig, J. M. Evidence for One-Dimensional Spin Order in  $V_3O_5$ . *Phys. Rev. B* **1980**, *21*, 154–158.
- (17) Rodríguez-Carvajal, J. Recent Advances in Magnetic Structure Determination by Neutron Powder Diffraction. *Phys. B* **1993**, *192*, 55–69.
- (18) Stokes, H. T.; Hatch, D. M.; Campbell, B. J. *ISODISTORT. ISOTROPY Software Suite*; Brigham Young University: [iso.byu.edu](http://iso.byu.edu). Accessed on the 2022-02-02.
- (19) Campbell, B. J.; Stokes, H. T.; Tanner, D. E.; Hatch, D. M. ISODISPLACE: A Web-Based Tool for Exploring Structural Distortions. *J. Appl. Crystallogr.* **2006**, *39*, 607–614.
- (20) Kresse, G.; Furthmüller, J. Efficient Iterative Schemes for *Ab Initio* Total-Energy Calculations Using a Plane-Wave Basis Set. *Phys. Rev. B* **1996**, *54*, 11169–11186.
- (21) Perdew, J. P.; Burke, K.; Ernzerhof, M. Generalized Gradient Approximation Made Simple. *Phys. Rev. Lett.* **1996**, *77*, 3865–3868.
- (22) Kresse, G.; Hafner, J. *Ab Initio* Molecular Dynamics for Liquid Metals. *Phys. Rev. B* **1993**, *47*, 558.
- (23) Azuma, M.; Chen, W. T.; Seki, H.; Czapski, M.; Olga, S.; Oka, K.; Mizumaki, M.; Watanuki, T.; Ishimatsu, N.; Kawamura, N.; Ishiwata, S.; Tucker, M. G.; Shimakawa, Y.; Attfield, J. P. Colossal Negative Thermal Expansion in  $BiNiO_3$  Induced by Intermetallic Charge Transfer. *Nat. Commun.* **2011**, *2*, 347.
- (24) Takenaka, K.; Takagi, H. Giant Negative Thermal Expansion in Ge-Doped Anti-Perovskite Manganese Nitrides. *Appl. Phys. Lett.* **2005**, *87*, 261902.
- (25) Takenaka, K. Progress of Research in Negative Thermal Expansion Materials: Paradigm Shift in the Control of Thermal Expansion. *Front. Chem.* **2018**, *6*, 267.
- (26) Whangbo, M.-H.; Koo, H.-J.; Dai, D. Spin Exchange Interactions and Magnetic Structures of Extended Magnetic Solids with Localized Spins: Theoretical Descriptions on Formal, Quantitative and Qualitative Levels. *J. Solid State Chem.* **2003**, *176*, 417–481.
- (27) Hatfield, W. E. New Magnetic and Structural Results for Uniformly Spaced, Alternatingly Spaced, and Ladder-like Copper (II) Linear Chain Compounds (Invited). *J. Appl. Phys.* **1981**, *52*, 1985–1990.
- (28) Kahn, O. *Molecular Magnetism*; VHC Publishers, Inc.: 1993.
- (29) Adda, C.; Lee, M.-H.; Kalcheim, Y.; Salev, P.; Rocco, R.; Vargas, N. M.; Ghazikhanian, N.; Li, C.-P.; Albright, G.; Rozenberg, M.; Schuller, I. K. Direct Observation of the Electrically Triggered Insulator-Metal Transition in  $V_3O_5$ . *Phys. Rev. X* **2022**, *12*, No. 011025.
- (30) Kucharczyk, D.; Niklewski, T. Accurate X-Ray Determination of the Lattice Parameters and the Thermal Expansion Coefficients of  $VO_2$  near the Transition Temperature. *J. Appl. Crystallogr.* **1979**, *12*, 370–373.
- (31) Song, X.; Sun, Z.; Huang, Q.; Rettenmayr, M.; Liu, X.; Seyring, M.; Li, G.; Rao, G.; Yin, F. Adjustable Zero Thermal Expansion in Antiperovskite Manganese Nitride. *Adv. Mater.* **2011**, *23*, 4690–4694.
- (32) McWhan, D. B.; Remeika, J. P. Metal-Insulator Transition in  $(V_{1-x}Cr_x)_2O_3$ . *Phys. Rev. B* **1970**, *2*, 3734–3750.
- (33) Pachoud, E.; Cumby, J.; Lithgow, C. T.; Attfield, J. P. Charge Order and Negative Thermal Expansion in  $V_2OPO_4$ . *J. Am. Chem. Soc.* **2018**, *140*, 636–641.



CAS BIOFINDER DISCOVERY PLATFORM™

## BRIDGE BIOLOGY AND CHEMISTRY FOR FASTER ANSWERS

Analyze target relationships,  
compound effects, and disease  
pathways

Explore the platform

**CAS**  
A Division of the  
American Chemical Society